

# Hydro-mechanical measurements and x-ray imaging of sheared crystalline rock fractures from EGS Collab experiments 1 & 2

Meng Meng<sup>1</sup>, Luke P Frash<sup>2</sup>, Wenfeng Li<sup>3</sup>, Nathan J Welch<sup>2</sup>, James William Carey<sup>4</sup>, Craig Ulrich<sup>5</sup>, and Timothy J Kneafsey<sup>6</sup>

<sup>1</sup>Los Alamos National Laboratory

<sup>2</sup>Los Alamos National Laboratory (DOE)

<sup>3</sup>Los Alamos National Lab

<sup>4</sup>Los Alamos National Laboratory

<sup>5</sup>Lawrence Berkeley National Laboratory

<sup>6</sup>Lawrence Berkeley Laboratory

November 22, 2022

## Abstract

Measuring hydro-mechanical properties of natural fractures is a prerequisite for optimizing hydraulic stimulation design and well placement. We completed experiments to characterize shear on natural fractures in schist, amphibolite, and rhyolite specimens drilled from EGS Collab Project's field sites at the Sanford Underground Research Facility (SURF) in South Dakota. A triaxial direct shear method and coupled x-ray imaging were used to perform hydroshearing and mechanical shearing at the site's in-situ stress conditions. This produced simultaneous measurements of fracture and matrix strength, permeability, stress-dependent aperture, dilation, and friction strength. Our results identified that only a subset of the natural fractures was weak enough for hydroshearing. Generally, hydroshearing increases fracture permeability by a factor of 10 or more and the enhancement is retainable over time. However, the shear slip does not always result in permeability enhancement. High content of phyllosilicates was found to associate with exceptionally weak fractures that also exhibited poor or even negative enhancement after stimulation. Combining our measurements with site data, we can predict that most observable fractures at the two EGS Collab sites do not meet the criteria for hydroshearing before tensile opening. In some cases, the visible fractures are low permeability and as strong as the adjacent rock. To induce hydroshearing before tensile opening, injection must target known weak and favorably oriented fractures with confirmed pre-existing permeability.

## Hosted file

supplement v7.docx available at <https://authorea.com/users/534312/articles/598447-hydro-mechanical-measurements-and-x-ray-imaging-of-sheared-crystalline-rock-fractures-from-egs-collab-experiments-1-2>

**Title: Hydro-mechanical measurements and x-ray imaging of sheared crystalline rock fractures from EGS Collab experiments 1 & 2**

**Authors:** Meng Meng<sup>1\*</sup>, Luke P. Frash<sup>1</sup>, Wenfeng Li<sup>1</sup>, Nathan J. Welch<sup>1</sup>, J. William Carey<sup>1</sup>, Craig Ulrich<sup>2</sup>, Timothy Kneafsey<sup>2</sup>

**Affiliations:**

<sup>1</sup>Los Alamos National Laboratory, Los Alamos, New Mexico, USA

<sup>2</sup>Lawrence Berkeley National Laboratory, Berkeley, California, USA

\*Corresponding author: Meng Meng ([mengm@lanl.gov](mailto:mengm@lanl.gov))

## **Key Points**

- Hydroshearing requires a natural fracture that is mechanically weak, hydraulically conductive, and favorably oriented.
- Fracture shear slip does not always result in permeability enhancement; when phyllosilicate rich, we observed decreasing permeability.
- Hydroshearing was demonstrated at the Experiment 1 site, but fractures appear likely to fail in tension before shear for Experiment 2.

## **Abstract**

Measuring hydro-mechanical properties of natural fractures is a prerequisite for optimizing hydraulic stimulation design and well placement. We completed experiments to characterize shear on natural fractures in schist, amphibolite, and rhyolite specimens drilled from EGS Collab Project's field sites at the Sanford Underground Research Facility (SURF) in South Dakota. A triaxial direct shear method and coupled x-ray imaging were used to perform hydroshearing and mechanical shearing at the site's in-situ stress conditions. This produced simultaneous measurements of fracture and matrix strength, permeability, stress-dependent aperture, dilation, and friction strength. Our results identified that only a subset of the natural fractures was weak enough for hydroshearing. Generally, hydroshearing increases fracture permeability by a factor of 10 or more and the enhancement is retainable over time. However, the shear slip does not always result in permeability enhancement. High content of phyllosilicates was found to associate with exceptionally weak fractures that also exhibited poor or even negative enhancement after stimulation. Combining our measurements with site data, we can predict that most observable fractures at the two EGS Collab sites do not meet the criteria for hydroshearing before tensile opening. In some cases, the visible fractures are low permeability and as strong as the adjacent rock. To induce hydroshearing before tensile opening, injection must target known weak and favorably oriented fractures with confirmed pre-existing permeability.

**Keywords:** triaxial direct shear; hydroshearing; enhanced geothermal systems; permeability; faults

## **1 Introduction**

Geothermal energy is attractive because it helps secure energy supply, mitigate climate change, and comply with future green energy policies. The GeoVision study estimates a potential 26-fold increase from 2019 geothermal energy production levels to 60 GW by 2050 in the United States (Hamm et al., 2019; Bromley et al., 2010; Dobson et al., 2017; Fan, 2020). To expand geothermal energy production, enhanced geothermal systems (EGS) is a key candidate technology (Tester et al., 2006). Hydroshearing, a process by which injection is used to increase pore pressure and thereby trigger slip along with pre-existing fractures, is one primary method for the rock stimulation that is required for EGS (McClure and

Horne, 2014, 2014b). Hydraulic fracturing is another primary stimulation method where higher injection pressures are used to create tensile fractures in addition to shear slip. However, fracture shear slip and its effects are challenging to predict for a given site.

Characterizing shear slip on natural fractures and faults can better inform predictions of natural or induced seismicity (Hincks et al., 2018), fault stability (Marone and Kilgore, 1993), and stimulated fracture fluid conductivity (Frash et al., 2017). Prior works have investigated frictional strength for stick-slip behavior (Leeman et al., 2016), permeability evolution during earthquake slip (Im et al., 2018), fault weakening induced by fluid injection (Scuderi et al., 2017), and scaling relations from shear fractures measured in the laboratory to the larger field situation (Frash et al., 2019a). Accurate site-specific characterization of shear fractures is especially important for geothermal energy applications where it is hoped that shear-propping (McClure and Horne, 2014b) could be a good alternative to the conventional proppants that are expected to perform poorly at high-stress and high-temperature conditions (Brinton, 2011; Li et al., 2021).

The crystalline and sedimentary rock that constitute most geothermal reservoirs are characterized by low permeability but often contain natural fractures (Dezayes et al., 2010). In this environment, conductive fractures are the dominant mechanism for fluid flow and heat extraction. The EGS Collab Project is investigating fracture-dominated high-stress crystalline-rock fluid-flow and the associated geophysical signatures using decameter scale (~10m) hydraulic stimulation experiments at Sanford Underground Research Facility (SURF) in South Dakota. This effort contributes to solving the above challenges as well as supporting future full-scale experiments at the Frontier Observatory for Research in Geothermal Energy (FORGE) in Milford, Utah. The EGS Collab project field sites include Experiment 1 (E1) at 1480 m depth and Experiment 2 (E2) at 1250 m depth. Here, we present site-specific geomechanical and hydrological testing of natural fractures. This information was used to aid the selection of favorable injection locations for hydroshearing and to improve diagnostic understanding of field observations.

We can gain additional value from our tests by considering its context with respect to prior works that investigated shear fracture strength and permeability behavior. Only limited experimental studies that characterize shear fractures have been reported, and even less work can be directly applied to field applications, mostly due to the common use of manufactured (saw-cut or polished) fractures or the lack of permeability measurements. The Supplementary Information includes a quick reference table summarizing this prior work. Most researchers found the permeability of granite can be increased by one to three orders of magnitude after shear. However, there are discrepancies where this enhancement was retainable in some cases (Witherspoon et al., 1980; Kluge et al., 2020; Ye and Ghassemi, 2018) but not retainable in other cases (Nemoto et al., 2008; Bauer et al., 2016). To elaborate, apart from Mitchell and

Faulkner (2008) and Kluge et al. (2020), most researchers used pre-cut flaws, either by saw-cut or a tensile splitting method, to produce planar fracture segments for experiments. These manufactured fractures do not replicate the roughness of natural fractures in the subsurface. In fact, the fracture roughness will strongly influence hydro-mechanical properties (Ye and Ghassemi, 2018). For the two studies that used in-situ created fractures (Mitchell and Faulkner 2008; Kluge et al. 2020), hydroshearing was not performed, and the hydro-mechanical behavior was tested only by mechanical shear. Furthermore, nearly all the previous research used only granite samples. In comparison, the EGS Collab field sites include naturally fractured schist, amphibolite, and rhyolite (Roggenthen, 2016; Kneafsey et al., 2019; Singh et al., 2019). None of the prior research studied hydroshearing or coupled hydro-mechanical properties for natural fractures through these crystalline rocks, so our work is the first to do so.

Different test methods were applied in the prior work, including direct shear, triaxial direct shear, and triaxial compression setups. To better understand the fundamental mechanisms of fracture fluid flow and best assist the EGS Collab Project's hydroshearing stimulation design, we determined that the test must include: (1) direct flow through the fracture that does not require in-series matrix diffusion; (2) stimulation of fractures at subsurface conditions while simultaneously measuring permeability; (3) hydroshearing attempts in the laboratory at replicated field stress conditions; (4) simultaneous mechanical, hydraulic, and geometry measurement without unloading; (5) targeting the actual site's natural fractures that were obtained from subsurface cores; and (6) timely presentation of results to the field site design team. For the previous studies, only (1) and (2) were met. Some researchers (Nemoto et al., 2008; Bauer et al. 2016; Sheng et al., 2018; Ye and Ghassemi, 2018) made great contributions to exploring mechanisms of hydroshearing, but the stress conditions were not reported as site-specific. In effect, EGS Collab provided a rare opportunity to combine site-specific measurements on targeted natural fractures to inform decision-making to design wells and future hydraulic stimulations.

Here, we present the hydro-mechanical properties of natural and created shear fractures in Poorman schist, Yates amphibolite, and rhyolite specimens from the EGS Collab E1 and E2 sites. This work used a triaxial direct shear method and integrated real-time x-ray imaging to meet all the above test requirements, including replicating in-situ stress conditions. We show that, unless a highly permeable and weak natural fracture is encountered by an injection well, the likely mechanism for hydraulic stimulation at the E2 site will initiate with tensile opening of a weak existing fracture that will then be subject to some shear offsetting that could self-prop the fracture. At the E1 site, our data helps to explain why a large pre-existing weak foliation fracture had a strong influence on flow at the site while the much more common infilled fractures had a negligible effect. Our measurements contributed to optimizing stimulation design for the ongoing EGS Collab project, including identifying well placements that encourage hydroshearing

and characterizing coupled shear fracture behavior for discrete fracture network models. In addition, we show that our measurements provide valuable insight into the hydroshearing process for any site.

## **2 Experimental Methods**

### **2.1 Samples Preparation from EGS Collab**

Our samples were cored from the EGS Collab sites on the 4100 and 4850 levels of SURF, at depths of 1250 and 1480 m, respectively. Two groups of field stimulation experiments were originally planned. Experiment 1 (E1) focused on hydraulic fracturing and was executed on the 4850 level. The forthcoming Experiment 2 (E2) is being designed to promote hydroshearing. Both sites were characterized for natural fracture locations and orientations, state of stress to a reasonable extent, and fracture hydro-mechanical properties. The key criterion for hydroshearing is the presence of permeable natural fractures, anisotropic principal stresses that impose shear on these fractures, and fracture strengths that are sufficiently weak so as to shear at pressures no greater than the hydraulic fracture propagation pressure (Singh et al., 2019). Both sites could potentially be suitable for hydroshearing simulation. The 4850 level site is located in the carbonate-rich, quartz-bearing phyllite of the upper Poorman schist (PS01 samples), whereas the 4100 level is located in the Yates amphibolite (YA02 samples) and is in close proximity to rhyolite intrusions.

Fig. 1a shows the specimens that we tested from the two experiment sites. These specimens intentionally targeted natural fractures so shear could be imposed across these localized features to measure the natural fracture properties. Furthermore, the samples isolated fractures that could reasonably be suspected of being weaker than the adjacent rock, as evident from core damage along similar features or locally elevated porosity (e.g., wormholes). PS01-03 and PS01-11 were foliation parallel and belonged to a south-east striking in-situ joint set. PS01-06, PS01-08, and PS01-09 included typical infilled mineralized field joints. PS01-11 contained a naturally pre-separated weak foliation that was separable before testing. PS01-11 is shown its state after shearing with a silicone rubber backing that was used to adapt this uniquely prepared slab sample into the cylindrical triaxial direct shear apparatus. YA02-01 is from an amphibolite-rhyolite contact that contained visible pores, unlike the typical rock matrix. YA02-02 is a dark mineral infilled fracture from the Yates amphibolite. YA02-03 is a white mineral-infilled amphibolite fracture. YA02-04 is a dark mineral infilled fracture from the rhyolite. YA02-05 contained a naturally fractured rhyolite fracture. After the experiments, the infilling minerals of the shear fractures were collected and sent for X-ray powder diffraction analysis (Table 1). The minerals are mainly composed of phyllosilicate, carbonate minerals, tectosilicate, and inosilicate minerals.

### **2.2 Facility description**

The experiments used the triaxial direct-shear method (Fig. 1) that was first developed by Carey et al. (2015a; 2015b; 2016) and modified by Frash et al. (2016; 2019c). Here, axial force induces direct-shear

stress on targeted fractures by two L-shaped steel pistons. Pore fluid pressure and flow along this fracture are induced by syringe pumps connected to each end of the sample. Permeability measurements were continuous over the entire experimental procedure. Geomechanical properties of the natural fractures were obtained by aligning the direct-shear load path with natural fractures. A ‘flow path splitter’ in the form of a twisted wire pair was used to avoid fluid channel blockage by small particles or debris generated by shearing the specimen. In-situ x-ray imaging permitted real-time viewing of sample deformation.

Unlike conventional tests, our triaxial direct-shear method meets all the requirements mentioned in the introduction. For those samples whose natural fracture was not located at the centerline of the end surface (YA02-03), a 0.2 mm thick segment-disk of stainless-steel sheet metal was inserted to ensure that the initial shear force was applied to only one side of the fracture for measurement of the fracture’s intact strength. Therefore, when axial compression is exerted on the piston, the natural fractures shear first. With additional shear displacement exceeding ~0.2 mm, the boundary conditions shift to fracture the matrix. Post-test inspection of samples using this method confirmed two end-to-end fractures. This solution achieved a double-measurement for each sample while also addressing tolerance challenges for coring. One shear stress peak gives strength of the natural fracture, and the other gives the strength of the matrix. We present our best interpretation of the resulting data utilizing all the information we had available.

### 2.3 In-situ stress simulation

In our direct shear test, we replicated the principal stress state measured from the E1 and E2 sites. For shear orientation, we assumed a 30° angle between the minimum principal stress and the normal to the fracture plane and a 60° angle from the maximum principal stress. It is unlikely that natural fractures will exactly match this orientation, but this enables the evaluation of hydroshearing potential at the actual site. Using Mohr-Coulomb and Terzaghi's effective stress theory (Eq. 1), this gives the stress parameters shown in Table 2 where the maximum potential in-situ shear stress for the lab tests was estimated at 9.7 MPa for E1 and 7.7 MPa for E2. The corresponding normal total stress was 29 MPa for E1 and 23 MPa for E2. It is important to note that Table 2 includes recent stress measurements from the E1 and E2 sites in addition to the numbers that were used for our laboratory tests. We relied on available data at the time of testing. More recent data are also included in Table 2.

$$\begin{aligned}\sigma'_n &= \sigma_n - p \\ \tau_n &= \sigma'_n \tan(\varphi) + c\end{aligned}\tag{1}$$

$$\sigma_n = \frac{\sigma_1 + \sigma_3}{2} - \frac{\sigma_1 - \sigma_3}{2} \cos(2\theta)$$

$$\tau_n = \frac{\sigma_1 - \sigma_3}{2} \sin(2\theta)$$

In the above,  $\sigma_n'$  is Terzaghi's effective normal stress,  $\sigma_n$  is normal stress,  $p$  is pore pressure,  $\tau_n$  is shear stress on the fracture,  $\varphi$  is contact friction angle,  $c$  is cohesion,  $\sigma_1$  is maximum principal compressive stress,  $\sigma_3$  is minimum principal compressive stress, and  $\theta$  is the angle between the minimum principal stress and the normal to the fracture plane.

Mechanical shear was completed using as much shear stress as needed to induce slip at the applied normal stress. Initial shearing was performed at the in-situ normal stress state for an optimally oriented fracture with respect to hydroshearing potential (Table 2). The use of multiple confining stresses after the first shear event gives a Mohr-Coulomb type failure envelope from the triaxial direct-shear test method.

The potential shear stress at this site depends on the orientation of the shear fracture. Based on Eq. (1), the minimum injection pressure ( $P_{ic}$ ) when shear could be triggered on an optimally oriented natural fracture can be estimated by the following equation:

$$P_{ic} = 0.5(\sigma_1 + \sigma_3) + \frac{C}{\tan(\varphi)} - 0.5(\sigma_1 - \sigma_3)/\sin(\varphi) \quad (2)$$

## 2.4 Experimental procedure

The experiments consisted of shearing the naturally fractured samples while simultaneously measuring hydro-mechanical properties and fracture geometry. Due to the significant differences of each sample and progressive understanding of their performance, some procedures changes were required. This resulted in the specific procedures for each test varying, but the general procedures are as follows:

- (1) Set up the sample as Fig. 1, and increase the confining pressure to the target values, 29 MPa for PS01 samples and 23 MPa for YA02 samples. Maintain a pore pressure difference and measure flow rate between the upper and lower ends of the sample to observe specimen permeability.
- (2) Apply the direct shear stress at the in-situ stress value, 9.7 MPa for PS01 samples and 7.7 MPa for YA02 samples. Attempt hydroshearing by increasing the pore pressure to a value slightly lower than the confining pressure to avoid jacket bursting. If axial displacement increment and/or a shear stress drop were observed during pore pressure increase, it meant that hydroshearing had occurred.



- (3) Pore pressure was reduced to original values, and mechanical shearing was performed by increasing the shear stress via axial piston displacement at a steady rate until mechanical failure is observed. This event was indicated by a peak or plateau in shear stress as shear displacement increased.
- (4) Optionally, maintain confining pressure and attempt to hydroshearing again by increasing the pore pressure. Axial displacement increments during increasing of pore pressure meant hydroshearing had occurred.
- (5) Perform additional mechanical or hydroshearing steps under the same or different confining pressure to measure the hydro-mechanical properties of the fractured specimen. Properties of interest included shear strength and permeability as a function of displacement and measurement of the shear strength. The prior requires a constant confining stress, while the latter requires changing confining stress.
- (6) Cycle the confining pressure to a high and then low value for the measurement of permeability and fracture aperture as a function of confining pressure. This provides a key input for coupled fracture flow and geomechanical models.
- (7) Perform dynamic shearing with simultaneous changing of confining pressure and axial displacement to larger displacement magnitudes. This procedure provides information about the shear strength and insight into the transient and variable behavior of permeability as a function of increasing shear damage. This procedure had a high chance of causing confining jacket failure due to dilated apertures often exceeding 2 mm, so this test was reserved for the last stage of testing.

## 2.5 Permeability calculation

The value of fracture permeability depends on the geometry that is used to define the flow path length and cross-sectional area. In this study, we report the specimen bulk permeability as calculated by:

$$k = \frac{4Q\mu L}{\pi D^2 \Delta P} \quad (3)$$

Where,  $Q$  is volumetric flow rate,  $\mu$  is dynamic viscosity,  $L$  is sample initial length,  $D$  is sample diameter, and  $\Delta P$  is the pressure drop across the fracture. The values for this measurement are populated using inlet and outlet pressures and flow rates to provide an uncertainty estimate for the calculated permeability.

## 3 Results and analysis

Hydro-mechanical measurements were completed for PS01-03, PS01-06, PS01-08, PS01-09, PS01-11, YA02-01, YA02-02, YA02-03, YA02-04, and YA02-05. We describe the minimum representative subset

of these tests as needed to explain the compiled fracture parameters that we later present. The supplementary information gives additional data for the other tests.

### **3.1 Example triaxial direct-shear test for naturally fractured Poorman schist (PS01-06)**

Fig. 2 shows results from shearing an initially intact infilled natural-fracture Poorman schist (E1) sample. This test obtained geometry measurements by x-ray imaging, using methods described in Frash et al. (2019a). Sequentially, this experiment included: (1) an intact fracture hydroshearing attempt, (2) mechanical shearing at in-situ confining stress, (3) a second hydroshearing attempt, (4) mechanical shearing at different effective confining stresses via changing pore pressure, (5) stress-dependent permeability, (6) in-situ x-ray microtomography scan, and (7) dynamic shear test. X-ray images provided valuable insights and confirmation of success or failure that conventional measurements are not able to provide, as exhibited by the radiographs of the sample at different times. At the beginning of the test, we can see that the sample was intact and the natural fracture is invisible to x-rays because it was completely infilled (c.f. Fig. 1a).

The initial hydroshearing attempt involved increasing the inlet pore pressure to 28 MPa, which was limited to be slightly less than the confining pressure of 29 MPa to prevent sleeve failure. However, the sample permeability was low, so the fluid pressure was unable to promptly diffuse across the sample. This is an unfavorable condition for hydroshearing at field conditions because pressure must be able to permeate into the natural fracture to induce hydroshearing. Next, we increased the outlet pore pressure to 28 MPa and permitted time for pressure permeation, 32 minutes in total. No shear stress drop, permeability increase, or shear slip was observed, which indicates that hydroshearing did not occur. The x-ray imaging confirmed that no shear stimulation had occurred. After that, mechanical shear was performed and the sample sheared at a direct-shear strength of 58 MPa. A clear shear fracture was generated, connecting both ends of the sample (Fig. 2d). Sample permeability increased from less than  $10^{-3}$  mD to the magnitude of  $10^{-1}$  mD. Radial dilation increased from 0.03 mm to 0.14 mm.

With the newly created shear fracture returned to in-situ conditions, hydroshearing was attempted again by increasing the inlet pore pressure. With the increased hydraulic conductivity from mechanical shearing, the pore pressure at the outlet now more promptly matched the inlet pore pressure. When the pore pressure neared 20 MPa, hydroshearing was confirmed by increased axial displacement, aperture dilation, permeability increase, and shear stress drop. The sample hydro-sheared from 0.3 mm to 0.7 mm, dilation aperture increased from 0.14 mm to 0.29 mm, and permeability increased from  $10^{-1}$  mD to a maximum of 10 mD. The corresponding x-ray radiographs show increasing damage from hydroshearing. After shearing, the fracture permeability retained a 25-fold permeability enhancement (1 mD compared

with 0.04 mD). The retained permeability is similar to prior findings (Ye and Ghassemi 2018, Kluge et al. 2020) and confirms the ability for hydroshearing to stimulate fractures in the Poorman schist.

After hydroshearing, we further mechanically sheared the sample at different effective confining stresses. This provides a measure of residual fracture cohesion and internal friction angle. Finally, the stress-dependent properties (e.g., permeability) were measured, and dynamic shear was performed. Dynamic shear provides another measurement for the relationship between shear stress and confining pressure, and these values closely agreed with the stepwise measurement, as to be described in later sections. Observations of this type were used to modify the experiment procedures for follow-on tests to better target the many different parameters of interest. Our ultimate goal here was to identify natural fractures that were capable of hydroshearing at the EGS Collab E1 and E2 while also obtaining measurements of the fracture properties that are needed for predictive models.

### **3.2 Mechanical properties of shear fractures**

All fractures were sheared under multiple confining pressures and key values are summarized in Table 3. Additional detail regarding each test is provided in the Supporting Information. Based on our results, we are able to estimate Mohr-Coulomb type failure curves for the specimens from the EGS Collab E1 and E2 sites. This interpretation is also shown in Fig. 3.

Aside from the weakest specimens PS01-11 and YA02-05, the tested natural fractures from E1 and E2 were too strong for hydroshearing. For the exceptionally weak fracture of PS01-11, only 6 MPa of fluid pressure was theoretically needed to induce hydroshearing. In this test, hydroshearing occurred when the pore pressure reached 7.4 MPa (Fig. 3; Table 3). While slightly stronger, the weak YA02-05 specimen required 19.7 MPa to hydroshear, with a theoretical value of  $19.6 \pm 0.6$  MPa. In contrast, a pore pressure of 32 MPa was theoretically needed to hydroshear the PS01-09 specimen, so the actual hydroshearing could not occur. Overall, most of the infilled natural fractures and all of the in-situ created matrix fractures were too strong for hydroshearing before tensile fracturing at in-situ stress conditions. For these strong fractures, the critical pressure for hydroshearing was higher than the maximum pore pressure, as limited by the hydraulic fracturing pressure.

Microseismic data from EGS Collab E1 indicates that stimulation was dominated by approximately five planar fractures despite the high intensity of observable natural fractures in the site (Kneafsey et al., 2019). Instead, the fracture network was dominated by hydraulic fractures and shear stimulation of a limited number of weak natural fractures. These weak fractures are parallel to the foliation joint set (PS01-03 and PS01-11). Therefore, these triaxial direct-shear measurements paired with in-situ stress

measurements and well or core logs offer a path forwards to improve the predictions of future stimulation behavior.

For EGS Collab E2, only the naturally fractured rhyolite YA02-05 specimen was found to be susceptible to hydroshearing. This fracture had a critical pore pressure between 19.0 and 20.2 MPa which is less than the maximum pore pressure of 22.5 MPa, at which tensile hydraulic fracturing will occur (Table 3). Also, our results show that most natural fractures at the E2 site are weaker than the matrix. In combination, these results indicate that the likely mechanism for hydraulic stimulation at the E2 site will initiate with tensile opening of existing natural fractures. Since these fractures are unlikely to be perpendicular to the minimum principal stress, shear and shear propping may occur after the tensile opening. An exception would occur if a shear-oriented fracture similar to the very weak YA02-05 is encountered, but these seem to be rare at the E2 site.

### 3.3 Evolution of frictional strength

The apparent frictional strength ( $\mu$ ) of fractures is defined as the ratio of shear stress ( $\tau$ ) to effective confining pressure ( $\sigma'_n$ ). Analyzing apparent frictional strength helps to understand frictional stability and permeability evolution (Scuderi and Collettini 2016; Leeman et al. 2016; Fang et al. 2018b). Fig. 3 also shows the frictional strength for all tested samples during hydroshearing and mechanical shear. Several findings can be interpreted from these results.

First, the frictional strength is larger than 1 for all samples, except PS01-11 which targeted an exceptionally weak natural fracture. This frictional strength is much higher than conventional saw-cut tests or synthetic gouge filled fractures that exhibit apparent frictional strengths of around 0.5 (Scuderi and Collettini 2016; Leeman et al. 2016; Ye and Ghassemi 2019). Our measurements are also higher than the conventionally assumed frictional value of 0.6 to 0.8 for slip tendency analysis (Byerlee, 1978; Morris et al., 1996). Our results emphasize the importance of measuring natural fracture properties to separate the weak features from the strong. Core logs and wireline tools are useful for identifying fractures and joint sets, but these sets can contain strong mineralized natural fractures that will not affect fracture stimulation. From the data we now have for the EGS Collab sites, we now know that the vast majority of natural fractures in this site are strong fractures.

Second, hydroshearing can reduce the frictional strength of fractures. For example, under the same total confining pressure, the frictional strength of PS01-06 drops from 1.04 to 0.85 after hydroshearing. However, the frictional strength only dropped slightly due to hydroshearing for PS01-08 (from 1.23 to

1.20) and YA02-05 (from 1.10 to 1.06). This magnitude of this decrease appears to depend on the cumulative shear displacement of the fractures. The specimen PS01-06 with the larger frictional strength drop was sheared for 0.35 mm, while PS01-08 and YA02-05 were only sheared for 0.035 mm. During hydroshearing, pore fluids dilate the fractures and decrease effective normal stresses. This can help to reduce asperity damage and decrease the effect of small-scale asperity interlocking, effectively lubricating the fractures. When injected pore pressure is reduced to the original low level, the fracture surface cannot retain the strong interlocking performance antecedent to hydroshearing due to irreversible fracture dilation (Fig. 2), reduction of solid-to-solid contact area, and fracture degradation. In effect, it appears that hydroshearing has a strong tendency for strain-weakening behavior and increased conductivity enhancement when compared to mechanical shearing.

Third, the frictional strength of an existing fracture gradually decreases as shear displacement increases. This could be attributed to the comminution of asperities and gouge for reduced effective surface roughness (Attache and Mellas 2017). It is unclear what scale-dependency could exist for this observed result (Frash, 2021). Post-test inspection of the samples confirmed fine particle generation inside of the shear fractures. Both mechanical shear and hydroshearing contribute to reduced frictional strength.

### **3.4 Permeability enhancement and mineral compositions**

The evolution of permeability during shearing is shown in Fig. 3 with key values summarized in Table 3. As shown in Fig. 3 and Table 3, the intact permeability of the natural fractures was less than  $10^{-3}$  mD, except for the pre-separated weak foliation PS01-11 and the pre-separated rhyolite fracture YA02-05. Hydroshearing for stimulation would be difficult or impossible for the low hydraulic conductivity fractures. After mechanical shear, the fractured specimens exhibited permeability greater than 0.01 mD (more than 10 times greater than original values), with the exception of the white mineral infilled amphibolite (YA02-03). For those samples with occurrence of hydroshearing, the fracture permeability generally increased to 10 times greater than values before hydroshearing. The only exception is the pre-fractured weak foliation PS01-11 sample where, instead of enhancing the permeability, the hydroshearing decreased the fracture permeability.

The hydraulic and mechanical properties of fractures can be linked to their mineralogical composition and properties (Davatzes et al., 2010; Cavailhes et al., 2013). Through XRD analysis of fracture materials in Table 1, we found that permeability enhancement is correlated with phyllosilicate (sheet mineral) content. A higher fraction of phyllosilicate associated with reduced permeability enhancement by mechanical shear and hydroshearing. This is consistent with prior work that observed fracture permeability decrease with phyllosilicate content and increase with tectosilicate content for shale rock (Fang et al., 2018b;

Zhang et al., 2020). A high content of phyllosilicates can act as membrane seals in permeable reservoirs (Cavailhes et al., 2013). In our work, the high content of phyllosilicates (77.3%) in PS01-11 associates with shear compaction (i.e., negative dilation) and permeability loss when sheared.

Gischig and Preisig (2015) estimated that stimulation methods need to increase the permeability of the deep reservoir to at least 0.01 to 1 mD for commercial EGS. Our laboratory shear test results indicate that the EGS Collab sites can achieve the fracture permeability that is appropriate to commercial EGS when suitably stimulated by fluid injection. However, the E1 field site required high injection pressures of around 30 MPa to sustain flow during circulation tests even though the same pressure was sufficient for hydraulic fracture propagation. In this case, the near well zone was dominated by tensile hydraulic fractures so it was likely that shear propping was negligible. Since no proppants were used, permeability in this tensile fracture zone could only be sustained by high-pressures (Kneafsey et al, 2019). This is a testament to the importance of promoting shear or including proppants to enable sustained flow at pressures below the hydraulic fracture limit. If an EGS system is to be designed using hydroshearing for the primary stimulation method, acknowledging the availability of fractures that are suitable for hydroshearing in the subsurface is extremely important. In a related notion, it would be a mistake to assume that an observable fracture implies a weak or permeable fracture.

### 3.5 Mechanical and hydraulic apertures at a different effective confining pressure

The mechanical and hydraulic aperture relationship has been studied extensively for unconventional shale rocks (Frash, 2016, 2019c; Li et al., 2020). Here, we explore the response of both mechanical and hydraulic fracture aperture to changing effective confining pressure in EGS Collab crystalline rocks. The mechanical aperture is the arithmetic average aperture of a fracture and the hydraulic aperture determines the flow behavior of a fracture as an alternative to permeability. In our experiments, the mechanical aperture was measured using x-ray radiography or displacement transducers. The effective hydraulic aperture relates the pressure and flow rate measurements to an equivalent smooth parallel plate aperture:

$$b_h = \sqrt[3]{\frac{12 \mu L Q}{\Delta P D}} \quad (4)$$

where  $b_h$  is the fracture effective hydraulic aperture,  $\mu$  is the fluid dynamic viscosity,  $L$  is the specimen length,  $Q$  is the volumetric flow rate,  $D$  is the specimen diameter (i.e., fracture width),  $\Delta P$  is the fluid pressure drop between the inlet and outlet ends of the specimen.

Generally, the hydraulic aperture is lower than the mechanical aperture because of the existence of contact areas within the fractures due to fracture roughness and tortuosity (Xiong et al., 2011). Both

mechanical aperture and hydraulic aperture are important for fluid flow, with the prior controlling porosity and the latter controlling flow rates (Li et al., 2020). However, mechanical aperture and hydraulic aperture are influenced by effective normal stress (Wu et al., 2017; Fang et al., 2018a). To interrelate these parameters, we first relate mechanical aperture with effective confining pressure (Barton et al., 1985) and then we relate mechanical aperture with hydraulic aperture (Witherspoon, 1980). Here, we consider two models for the relationship between the mechanical aperture and effective confining pressure, the Barton et al. (1985) model and an exponential decay model (Li et al., 2020).

Barton et al. model (1985):

$$b_d = b_{b0} - \frac{A \sigma'_n}{1 + B \sigma'_n} \quad (5)$$

where,  $\sigma'_n$  is the effective normal stress;  $b_{b0}$  is the initial mechanical aperture, which represents the mechanical aperture with zero effective normal stress;  $b_d$  is the mechanical aperture at a certain effective normal stress;  $A$  and  $B$  are fitted constants.

Exponential model (Li et al., 2020):

$$b_d = b_{e0} e^{-\alpha \sigma'_n} \quad (6)$$

where  $b_{e0}$  is the initial mechanical aperture, which represents the mechanical aperture with zero effective normal stress, and  $\alpha$  is the fitted compressibility coefficient.

After finding the mechanical aperture, we predict hydraulic aperture using the following relationship:

$$b_h = N b_d \quad (7)$$

where  $N$  is the ratio between hydraulic aperture and mechanical aperture, which we call a ‘modified Witherspoon factor’, paying tribute to the pioneering work by Witherspoon et al. (1980).

Fig. 4 and Table 4 provide the fitted results for the above models. While Barton et al. yields the better fit to the data, we prefer the exponential model for our subsequent estimation of the modified Witherspoon factor. Our selection stems from the inability to scale the Barton-Bandis model to fractures of different dimensions, whereas the exponential model is intuitively scalable (Li et al., 2020). Based on the fitted mechanical aperture from the exponential model, we fit the modified Witherspoon factor to the measured mechanical and hydraulic apertures. Renshaw (1995) points out that the ratio between mechanical and

hydraulic aperture depends on fracture surface roughness. Eq. 7 empirically includes these higher-order effects in a simple way for modeling coupled effects.

Hydraulic and mechanical aperture both decrease with increasing confining pressure, but the fractures maintain an aperture even at very high confining pressure. We also find that the mechanical aperture is dependent on the stress history but the hydraulic aperture dependence on stress history is less obvious. Similarly, Witherspoon et al. (1980) and Kluge et al. (2020) found pressure cycling led to reversible permeability changes, whereas Ye and Ghassemi (2008) found the permeability change is irreversible. This behavior appears to indicate a dependency of stress-dependent aperture behavior on material properties and surface roughness. Furthermore, if the stress history caused degradation of fracture asperities, the permeability is more likely to be irreversible.

A key observation from these results is that  $b_h/b_d$  ratios can be orders of magnitude smaller than 1. The prior publications that used saw-cut fractures as opposed to natural fractures were unable to see this result (Witherspoon et al., 1980; Zimmerman and Bodvarsson et al., 1996; Nemoto et al., 2008; Ye and Ghassemi, 2019), so these earlier works report  $b_h/b_d$  ratios closer to 1. This finding highlights the need to consider actual fracture properties, inclusive of roughness effects, in order to accurately model fracture-dominated subsurface flow and transport.

#### **4 Application to EGS Collab Experiment 1 & 2 Sites**

The hydroshearing potential depends not only on the hydro-mechanical properties of natural fractures, but also the in-situ stress and orientation of fractures. Based on our measurements, the only samples that were weak enough for hydroshearing before tensile opening were PS01-11 and YA02-05. If we assume that these properties could exist on fractures of any orientation, we can use the strength values for these fractures (Table 3) to evaluate slip tendency using stereoplots (Fig. 5). This figure shows the minimum fluid pressure that can induce hydroshearing for fractures having different orientations. Here, we immediately see that hydroshearing should be relatively easy at the E1 site but is likely to be more difficult at the E2 site because of the higher required pressures that are predicted for the E2 site.

Next, we can additionally consider in-situ fracture orientations observed from well logs (Table 2). For context, we also include this information using the poles (i.e., normal vectors) of the respective features. These fracture sets were identified by acoustic televiewer and optical well logs. Here, we find that PS01-11 (E1) aligns with the foliation which has an orientation where shear slip could occur at pressures of only 10 to 15 MPa, which is much less than the observed hydraulic fracturing pressure of 28 to 31 MPa. However, YA02-05 (E2) aligns with the tensile hydraulic fractures orientations that were produced by the



DFIT tests so its critical pressure is nearly equal to the hydraulic fracturing pressure of 15 to 35 MPa that was measured at this site. Therefore, it appears that this fracture will have only minimal shear stress on it. Even though it is weak, the YA02-05 fracture is likely to fail in tension before shear. To hydroshear at the E2 site, it will be crucial that fractures at least as weak as YA02-05 are intersected and that these fractures are oriented for shear and permeable.

At the E1 site, this analysis reveals that Joint Set 1, Joint Set 2, and the foliation are suitably oriented for shearing. However, the infilled naturally fractured samples were very low permeability and quite strong before mechanical shearing. Therefore, most of these fractures are unlikely to hydroshear or even influence hydraulic fracture propagation. During actual field stimulation, microseismic monitoring (Schoenball, 2019) combined with distributed temperature sensing (DTS) confirmed stimulation of hydraulic fractures, a fracture between Joint Sets 1 and 3, and the foliation at the E1 site. It is important to note that, in the E1 site, stimulation started with a high pressure hydraulic fracture (nominally 31 MPa) and that the theoretically required stimulation pressure for some natural fractures was less than this value. This situation produces a dynamic scenario where a growing hydraulic fracture can trigger the hydroshearing of natural fractures.

At the E2 site, the hydraulic fracture pressure (i.e., maximum pore pressure) was highly variable ranging from 15 to 35 MPa (Ingraham et al., 2020). Here, Joint Set 2, Joint Set 3, and the foliation have favorable fracture orientations for hydroshearing so the E2 site has some potential for shear at the higher pressures. However, due to lower total stresses, the potential shear stress is lower at the E2 site than for the E1 site. At the same time, the weakest fractures at the E2 site were considerably stronger than the weakest fractures at the E1 site. In the rhyolite, where YA02-05 was extracted, DFIT tests indicated low minimum principal stresses in the range of 15 to 19 MPa (Ingraham et al., 2020). The amphibolite minimum stresses were in the range of 20 to 30 MPa. Therefore, the higher stress anisotropy in the rhyolite will yield increased potential shear stresses relative to the amphibolite. This presents a complicated scenario for analysis, but it appears to indicate that hydroshearing could be most easily achieved in the rhyolite, whereas the amphibolite would be more challenging. Regardless, our work did not find any fractures meeting the criteria for hydroshear at the E2 site. Instead, this work indicates that the natural fractures in the E2 site, both for rhyolite or amphibolite, are weaker than the matrix so they are likely to open in tension before the matrix hydraulic fractures. Since these fractures are not perpendicular to the minimum principal stress, they will then likely be subject to some minor shearing. Thus, there is a potential for shear propping after the natural fractures are stimulated.

## 5 Conclusion

We completed hydro-mechanical measurements on crystalline rock specimens from the EGS Collab field sites at SURF. These tests targeted natural fractures in the Experiment 1 (E1) site on 4850 level (Poorman schist) and the Experiment 2 (E2) site on the 4100 level (Yates amphibolite and rhyolite). This work was performed to aid the design of well placement and selection of injection locations for hydraulic fracturing and/or hydroshearing. This work also provided measurements of fracture properties to better characterize the coupled hydro-mechanical behavior of fractures for models.

With respect to fracture strength, our measurements identify two exceptionally weak fracture sets that could be hydro-sheared without need to first tensile fracture or mechanically shear these features. Initiating hydroshearing in-situ requires the combination of shear stress (i.e., stress anisotropy), a favorably oriented natural fracture, a mechanically weak fracture, and pre-existing hydraulic conductivity. This may appear to be strict and limiting, but this condition was met at the E1 site for foliation parallel fractures. At the E2 site, no suitable fractures for hydroshearing were identified but, unlike for the E1 site, most natural fractures were weaker than the rock matrix. Thus, the E2 site has a potential for natural fractures to fail in tension and then be subject to shear offsetting for shear propping.

With respect to shearing to enhance permeability, most natural fractures at the EGS Collab sites initially had low permeability at less than  $10^{-3}$  mD. After shearing, the fracture permeability increased in most cases, often to 0.01 mD or higher. However, one sample that was phyllosilicate rich exhibited shear compaction and permeability reduction after shearing. Therefore, it should not be assumed that shear stimulation will always result with higher hydraulic conductivity.

With respect to natural fractures versus saw-cut samples, our rough-surfaced natural fractures exhibited large differences between mechanical aperture and hydraulic aperture, which we express using modified Witherspoon factors that were often measured to be less than 0.05. This factors for saw-cut samples tends to be greater than 0.8. Also, our measurements of apparent frictional strength were typically greater than 1 while saw-cut samples tend to be close to 0.5. Our lowest measured apparent frictional strength was 0.3 for a phyllosilicate rich fracture. In short, the ranges of these values are significantly more expanded than what prior works would indicate.

With respect to stress-dependent aperture, we used an exponential model to relate effective normal stress to mechanical aperture and hydraulic aperture (i.e., permeability). Here, we observe that a constant modified Witherspoon factor succeeds reasonably well at fitting the hydraulic aperture data simultaneously with the mechanical aperture data. The compressibility of our crystalline rock samples in

our exponential aperture model ranges between  $-0.0145$  and  $-0.0068 \text{ MPa}^{-1}$ . For more ductile shale rocks, values less than  $-0.089 \text{ MPa}^{-1}$  have been observed.

Overall, this work provides useful new insights about the competition between hydroshearing of natural fractures, tensile opening of existing fractures, and hydraulic fracturing of matrix rock. Our measurements provided useful data for EGS Collab design decisions and diagnostics. If applied at other sites, targeted triaxial direct-shear tests combined with in-situ stress measurements could provide valuable constraints for predicting the effects of hydraulic stimulation in fracture-dominated rock systems.

## Acknowledgements

This work is supported by Department of Energy (DOE) Basic Energy Sciences under FWP LANLE3W1. Additional support was provided by the EGS Collab Project from the U.S. Department of Energy, Office of Energy Efficiency and Renewable Energy (EERE), Geothermal Technologies Office (GTO) under Contract No. DE-AC52-06NA25396 with Los Alamos National Laboratory, led by Contract No. DEAC02-05CH11231 with Lawrence Berkeley National Laboratory. Research supporting this work took place in whole or in part at the Sanford Underground Research Facility in Lead, South Dakota. The assistance of the Sanford Underground Research Facility and its personnel in providing physical access and general logistical and technical support is gratefully acknowledged. Data supporting this work is included here in this manuscript and/or in the Supporting Information.

EGS Collab Team: J. Ajo-Franklin<sup>LBNL,Rice</sup>, T. Baumgartner<sup>SURF</sup>, K. Beckers<sup>NREL</sup>, D. Blankenship<sup>SNL</sup>, A. Bonneville<sup>PNNL</sup>, L. Boyd<sup>DOE</sup>, S. Brown<sup>NETL</sup>, J.A. Burghardt<sup>PNNL</sup>, C. Chai<sup>ORNL</sup>, A. Chakravarty<sup>LBNL</sup>, T. Chen<sup>LANL</sup>, Y. Chen<sup>LANL</sup>, B. Chi<sup>Rice</sup>, K. Condon<sup>UWM</sup>, P.J. Cook<sup>LBNL</sup>, D. Crandall<sup>NETL</sup>, P.F. Dobson<sup>LBNL</sup>, T. Doe<sup>TDG</sup>, C.A. Doughty<sup>LBNL</sup>, D. Elsworth<sup>Penn</sup>, J. Feldman<sup>SNL</sup>, Z. Feng<sup>LANL</sup>, A. Foris<sup>SNL</sup>, L.P. Frash<sup>LANL</sup>, Z. Frone<sup>DOE</sup>, P. Fu<sup>LLNL</sup>, K. Gao<sup>LANL</sup>, A. Ghassemi<sup>OU</sup>, Y. Guglielmi<sup>LBNL</sup>, B. Haimson<sup>UWM</sup>, A. Hawkins<sup>Stanford</sup>, J. Heise<sup>SURF</sup>, C. Hopp<sup>LBNL</sup>, M. Horn<sup>SURF</sup>, R.N. Horne<sup>Stanford</sup>, J. Horner<sup>PNNL</sup>, M. Hu<sup>LBNL</sup>, H. Huang<sup>former INL</sup>, L. Huang<sup>LANL</sup>, K.J. Im<sup>Penn</sup>, M. Ingraham<sup>SNL</sup>, E. Jafarov<sup>LANL</sup>, R.S. Jayne<sup>LBNL</sup>, T.C. Johnson<sup>PNNL</sup>, S.E. Johnson<sup>LBNL</sup>, B. Johnston<sup>NREL</sup>, S. Karra<sup>LANL</sup>, K. Kim<sup>LBNL</sup>, D.K. King<sup>SNL</sup>, T. Kneafsey<sup>LBNL</sup>, H. Knox<sup>PNNL</sup>, J. Knox<sup>PNNL</sup>, D. Kumar<sup>OU</sup>, K. Kutun<sup>CSM</sup>, M. Lee<sup>SNL</sup>, D. Li<sup>LANL</sup>, J. Li<sup>LANL</sup>, K. Li<sup>Stanford</sup>, Z. Li<sup>Penn</sup>, M. Maceira<sup>ORNL</sup>, P. Mackey<sup>NETL</sup>, N. Makedonska<sup>LANL</sup>, C.J. Marone<sup>Penn</sup>, E. Mattson<sup>MH</sup>, M.W. McClure<sup>RF</sup>, J. McLennan<sup>UU</sup>, T. McLing<sup>INL</sup>, C. Medler<sup>SDSMT</sup>, R.J. Mellors<sup>LLNL</sup>, E. Metcalfe<sup>DOE</sup>, J. Miskimins<sup>CSM</sup>, J. Moore<sup>NETL</sup>, C.E. Morency<sup>LLNL</sup>, J.P. Morris<sup>LLNL</sup>, T. Myers<sup>SNL</sup>, S. Nakagawa<sup>LBNL</sup>, G. Neupane<sup>INL</sup>, G. Newman<sup>LBNL</sup>, A. Nieto<sup>DOE</sup>, T. Paronish<sup>NETL</sup>, R. Pawar<sup>LANL</sup>, P. Petrov<sup>LBNL</sup>, B. Pietzyk<sup>SURF</sup>, R. Podgorney<sup>INL</sup>, Y. Polsky<sup>ORNL</sup>, J. Pope<sup>SNL</sup>, S. Porse<sup>DOE</sup>, J.C. Primo<sup>LBNL</sup>, C. Reimers<sup>SDSMT</sup>, B.Q. Roberts<sup>PNNL</sup>, M. Robertson<sup>LBNL</sup>, V. Rodriguez-Tribaldos<sup>LBNL</sup>, W. Roggenthen<sup>SDSMT</sup>, J. Rutqvist<sup>LBNL</sup>, D. Rynders<sup>SURF</sup>, M. Schoenball<sup>NAGRA</sup>, P. Schwering<sup>SNL</sup>,

V. Sesetty<sup>OU</sup>, C.S. Sherman<sup>LLNL</sup>, A. Singh<sup>Stanford</sup>, M.M. Smith<sup>LLNL</sup>, H. Sone<sup>UWM</sup>, E.L. Sonnenthal<sup>LBNL</sup>, F.A. Soom<sup>LBNL</sup>, D.P. Sprinkle<sup>PNNL</sup>, S. Sprinkle<sup>LBNL</sup>, C.E. Strickland<sup>PNNL</sup>, J. Su<sup>SNL</sup>, D. Templeton<sup>LLNL</sup>, J.N. Thomle<sup>PNNL</sup>, C. Ulrich<sup>LBNL</sup>, N. Uzunlar<sup>SDSMT</sup>, A. Vachaparampil<sup>OU</sup>, C.A. Valladao<sup>LBNL</sup>, W. Vandermeer<sup>DOE</sup>, G. Vandine<sup>SURF</sup>, D. Vardiman<sup>SURF</sup>, V.R. Vermeul<sup>PNNL</sup>, J.L. Wagoner<sup>LLNL</sup>, H.F. Wang<sup>UWM</sup>, J. Weers<sup>NREL</sup>, N. Welch<sup>LANL</sup>, J. White, M.D. White<sup>PNNL</sup>, P. Winterfeld<sup>CSM</sup>, T. Wood<sup>LBNL</sup>, S. Workman<sup>NETL</sup>, H. Wu<sup>LLNL</sup>, Y.S. Wu<sup>CSM</sup>, E.C. Yildirim<sup>Penn</sup>, Y. Zhang<sup>Stanford</sup>, Y.Q. Zhang<sup>LBNL</sup>, Q. Zhou<sup>LBNL</sup>, M.D. Zoback<sup>Stanford</sup>

## References

- Anderson, J. G., Wesnousky, S. G., & Stirling, M. W. (1996). Earthquake size as a function of fault slip rate. *Bulletin of the Seismological Society of America*, 86(3), 683-690.
- Attache, S., & Mellas, M. (2017). Numerical study of large-scale pull-out test of horizontal corrugated strips. *International Journal of Geotechnical Engineering*, 14(1): 1-9.
- Barton N, Bandis S, & Bakhtar K. (1985) Strength deformation and conductivity coupling of rock joints. *International Journal of Rock Mechanics and Mining Sciences & Geomechanics Abstracts*, 22(3):121–140. [https://doi.org/10.1016/0148-9062\(85\)93227-9](https://doi.org/10.1016/0148-9062(85)93227-9).
- Bauer, S. J., Huang, K., Chen, Q., Ghassemi, A., & Barrow, P. C. (2019). Experimental and Numerical Investigation of Hydro-Thermally Induced Shear Stimulation. Paper presented at the 50th U.S. Rock Mechanics/Geomechanics Symposium, Houston, United States.
- Brenguier, F., Campillo, M., Hadziioannou, C., Shapiro, N. M., Nadeau, R. M., & Larose, E. (2008). Postseismic relaxation along the San Andreas fault at Parkfield from continuous seismological observations. *Science*, 321(5895): 1478-1481.
- Brinton, D. (2011). Issues surrounding fracturing of geothermal systems – predicting thermal conductivity of reservoir rocks and evaluating performance of fracture proppants, (MS Thesis). Salt Lake City: University of Utah.
- Bromley, C. J., Mongillo, M., Hiriart, G., et al. (2010). Contribution of geothermal energy to climate change mitigation: the IPCC renewable energy report. Paper presented at Proceedings World Geothermal Congress 2010, Bali, Indonesia.
- Byerlee, J. 1978. Friction of rocks. *Pure and Applied Geophysics*: 116: 615-626.
- Carey, J. W., Lei, Z., Rougier, E., Mori, H., & Viswanathan, H.S.: Fracture-permeability behavior of shale. *Journal of Unconventional Oil and Gas Resources*, 11, 27-43 (2015a).
- Carey, J. W., Rougier, E., Lei, Z., & Viswanathan, H. Experimental investigation of fracturing of shale with water. Paper presented at proceedings of the 49th US Rock Mechanics / Geomechanics Symposium, San Francisco, United States.
- Carey, J. W., Frash, L. P., Viswanathan, H. S. Dynamic triaxial study of direct shear fracturing and precipitation-induced transient permeability observed by in situ x-ray radiography. Paper presented at proceedings of the 50th U.S. Rock Mechanics/Geomechanics Symposium, Houston, United States.
- Cavailhes, T., Soliva, R., Labaume, P., Wibberley, C., Sizun, J. P., Gout, C., Charpentier D., Chauvet A., Scalabrino B., & Buatier, M. (2013). Phyllosilicates formation in faults rocks: Implications for dormant fault–sealing potential and fault strength in the upper crust. *Geophysical Research Letters*, 40(16): 4272-4278.
- Chen, Z., Narayan, S. P., Yang, Z., & Rahman, S. S. (2000). An experimental investigation of hydraulic behaviour of fractures and joints in granitic rock. *International Journal of Rock Mechanics and Mining Sciences*, 37(7): 1061-1071.

- Davatzes, N.C. and S. H. Hickman. (2010). The Feedback Between Stress, Faulting, and Fluid Flow: Lessons from the Coso Geothermal Field, CA, USA. Paper presented at proceedings World Geothermal Congress 2010, Bali, Indonesia.
- Dezayes, C., Genter, A., & Valley, B. (2010). Structure of the low permeable naturally fractured geothermal reservoir at Soultz. *Comptes Rendus Geoscience*, 342(7-8): 517-530.
- Dobson, P., Kneafsey, T. J., Blankenship, et al. (2017). An introduction to the EGS Collab Project. *GRC Transactions*, 41: 837-849.
- Esaki, T., Du, S., Mitani, Y., Ikusada, K., and Jing, L. (1999). Development of a shear-flow test apparatus and determination of coupled properties for a single rock joint. *International Journal of Rock Mechanics and Mining Sciences*, 36(5): 641-650.
- Fan, Melissa. (2020). Digging Deeper into Enhanced Geothermal Systems: Techno-Economic Simulation of EGS Electricity Generation Development. (Thesis). Princeton: Princeton University.
- Fang, Y., Elsworth, D., Ishibashi, T., & Zhang, F. (2018a). Permeability evolution and frictional stability of fabricated fractures with specified roughness. *Journal of Geophysical Research: Solid Earth*, 123(11): 9355-9375.
- Fang, Y., Elsworth, D., Wang, C., & Jia, Y. (2018b). Mineralogical controls on frictional strength, stability, and shear permeability evolution of fractures. *Journal of Geophysical Research: Solid Earth*, 123(5): 3549-3563.
- Frash, L. P., Carey, J. W., Lei, Z., Rougier, E., Ickes, T., & Viswanathan, H. S. (2016). High-stress triaxial direct-shear fracturing of Utica shale and in situ X-ray microtomography with permeability measurement. *Journal of Geophysical Research: Solid Earth*, 121(7): 5493-5508.
- Frash, L. P., Carey, J. W., Ickes, T., & Viswanathan, H. (2017). Caprock integrity susceptibility to permeable fracture creation. *International Journal of Greenhouse Gas Control*, 64: 60-72.
- Frash, L. P., Carey, J. W., & Welch, N. J. (2019a). Scalable En Echelon Shear-Fracture Aperture-Roughness Mechanism: Theory, Validation, and Implications. *Journal of Geophysical Research: Solid Earth*, 124(1): 957-977.
- Frash, L. P., Carey, J. W., Welch, N. J., & EGS Collab Team. 2019b. EGS Collab Experiment 1 Geomechanical and Hydrological Properties by Triaxial Direct Shear. Paper presented at 44th Workshop on Geothermal Reservoir Engineering. California, United States.
- Frash, L. P., Welch, N. J., Carey, J. W., & EGS Collab Team. 2019c. Geomechanical evaluation of natural shear fractures in the EGS Collab Experiment 1 test bed. Paper presented at the 53rd U.S. Rock Mechanics/Geomechanics Symposium, New York City, United States.
- Frash, L.P., Welch, N.J., Meng, M., Li, W., Carey, J.W. (2021) A scaling relationship for fracture permeability after slip. Paper presented at proceedings of the 55th US Rock Mechanics/Geomechanics Symposium, Houston, United States.
- Gentier, S., E. Lamontagne, G. Archambault, & J. Riss (1997), Anisotropy of flow in a fracture undergoing shear and its relationship to the direction of shearing and injection pressure, *International Journal of Rock Mechanics and Mining Sciences*, 34(3-4): 94.e1-94.e12.
- Gischig, V. S., & Preisig, G. (2015). Hydro-fracturing versus hydro-shearing: a critical assessment of two distinct reservoir stimulation mechanisms. Paper presented at 13th ISRM International Congress of Rock Mechanics. Montreal, Canada.
- Hamm, S. (2019). GeoVision: Harnessing the heat beneath our feet. U.S. Department of Energy.

- Hincks, T., Aspinall, W., Cooke, R., & Gernon, T. (2018). Oklahoma's induced seismicity strongly linked to wastewater injection depth. *Science*, 359(6381): 1251-1255.
- Im, K., Elsworth, D., & Fang, Y. (2018). The influence of preslip sealing on the permeability evolution of fractures and faults. *Geophysical Research Letters*, 45(1): 166-175.
- Ingraham, M.D., Schwering, P.C., Burghardt, J., Ulrich, C., Doe, T., Roggenthen, W.M., Reimers, C. 2020. Analysis of hydraulic fracturing on the 4100 level at the Sanford Underground Research Facility. Paper presented at the 54th U.S. Rock Mechanics/Geomechanics Symposium, physical event cancelled.
- Kneafsey, T. J., Dobson, P. F., Ajo-Franklin, J. B. et al. (2019). EGS Collab Project: status, tests, and data. Paper presented at Proceedings of the 53rd US Rock Mechanics/Geomechanics Symposium, New York City, United States.
- Li, W., Frash, L., Welch, N., Carey, J. W., Meng, M., & Wigand, M. (2020). Stress-Dependent Fracture Permeability Measurements and Implications for Shale Gas Production. *Fuel*. 2021: 119984.
- Li, Z., Elsworth, D., Wang, C., & EGS Collab. (2021). Constraining Maximum Event Magnitude during Injection-triggered Seismicity. *Nature Communications*, 12(1), 1528.
- Leeman, J. R., Saffer, D. M., Scuderi, M. M., & Marone, C. (2016). Laboratory observations of slow earthquakes and the spectrum of tectonic fault slip modes. *Nature communications*, 7(1): 1-6.
- Marone, C., & Kilgore, B. (1993). Scaling of the critical slip distance for seismic faulting with shear strain in fault zones. *Nature*, 362(6421): 618-621.
- McClure, M. W., & Horne, R. N. (2014a). Characterizing hydraulic fracturing with a tendency for shear stimulation test. Paper presented at SPE Annual Technical Conference and Exhibition, New Orleans, United States.
- McClure, M.W., & Horne, R.N. (2014b). An investigation of stimulation mechanisms in Enhanced Geothermal Systems. *International Journal of Rock Mechanics and Mining Sciences*. 72: 242-260.
- Morris, A., Ferrill, D.A., & Henderson, D.B. (1996). Slip-tendency analysis and fault reactivation. *Geology*, 24: 275-278.
- Kluge, C., Blöcher, G., Barnhoorn, A., & Bruhn, D. (2020). Hydraulic-mechanical properties of microfaults in granitic rock using the Punch-Through Shear test. *International Journal of Rock Mechanics and Mining Sciences*, 134: 104393.
- Nemoto, K., Moriya, H., Niitsuma, H., & Tsuchiya, N. (2008). Mechanical and hydraulic coupling of injection-induced slip along pre-existing fractures. *Geothermics*, 37(2): 157-172.
- Renshaw C. E. (1995). On the relationship between mechanical and hydraulic apertures in rough-walled fractures. *Journal of Geophysical Research: Solid Earth*, 100(B12): 24629–24636. <https://doi.org/10.1029/95JB02159>.
- Roggenthen, W. M. (2017). Geophysical and Geological Characterization of Core Materials in Support of the kISMET Experiment at the Sanford Underground Research Facility (SURF). Paper presented at 51st US Rock Mechanics/Geomechanics Symposium. San Francisco, Unites States.
- Schoenball, M., Ajo-Franklin, J., Blankenship, et al. (2019). Microseismic monitoring of meso-scale stimulations for the DOE EGS Collab project at the Sanford Underground Research Facility. Paper presented at Proceedings: 44th Workshop on Geothermal Reservoir Engineering, Stanford, United States.

- Scuderi, M. M., & Collettini, C. (2016). The role of fluid pressure in induced vs. triggered seismicity: Insights from rock deformation experiments on carbonates. *Scientific reports*, 6(1): 1-9.
- Scuderi, M. M., Collettini, C., & Marone, C. (2017). Frictional stability and earthquake triggering during fluid pressure stimulation of an experimental fault. *Earth and Planetary Science Letters*, 477: 84-96.
- Singh, A., Neupane, G., Dobson, P., et al. (2019). Slip Tendency Analysis of Fracture Networks to Determine Suitability of Candidate Testbeds for the EGS Collab Hydroshear Experiment. Idaho National Lab., Idaho Falls, United States.
- Tester, J.W., et al. (2006). The Future of Geothermal Energy: Impact of Enhanced Geothermal Systems (EGS) on the United States in the 21st Century. U. S. Department of Energy.
- Wu, W., Reece, J. S., Gensterblum, Y., & Zoback, M. D. (2017). Permeability evolution of slowly slipping faults in shale reservoirs. *Geophysical Research Letters*, 44(22): 11-368.
- Witherspoon PA, Wang JS, Iwai K, Gale JE. (1980). Validity of cubic law for fluid flow in a deformable rock fracture. *Water Resources Research*, 16(6): 1016–1024.
- Xiong, X., Li, B., Jiang, Y., Koyama, T., & Zhang, C. (2011). Experimental and numerical study of the geometrical and hydraulic characteristics of a single rock fracture during shear. *International Journal of Rock Mechanics and Mining Sciences*, 48(8): 1292-1302.
- Ye, Z., & Ghassemi, A. 2018. Injection-induced shear slip and permeability enhancement in granite fractures. *Journal of Geophysical Research: Solid Earth*, 123(10): 9009-9032.
- Zimmerman, R. W., & Bodvarsson, G. S. (1996). Hydraulic conductivity of rock fractures. *Transport in Porous Media*, 23(1): 1-30.
- Zhang, Q., Li, X., Bai, B., Pei, L., Shi, L., & Wang, Y. (2019). Development of a direct-shear apparatus coupling with high pore pressure and elevated temperatures. *Rock Mechanics and Rock Engineering*, 52(9): 3475-3484.

## Tables

Table 1. X-ray powder diffraction analysis of crystalline rock fracture infilling materials.

	Poorman Schist					Yates Amphibolite			
	PS 01-03	PS 01-06	PS 01-08	PS 01-09	PS 01-11	YA 02-01	YA 02-02	YA 02-03	YA 02-04
Tectosilicate									
Plagioclase	-	2.7	1.1	1.5	-	22.3	16.9	12.4	-
K-Feldspar	-	4.1	4.5	2.5	-	4.9	-	7.8	69.1
Quartz	19.9	25.9	28.5	26.4	11.0	12.3	8.5	24.5	26.7
TOTAL	19.9	32.7	34.1	30.4	11	39.5	25.4	44.7	95.8
Carbonate mineral									
Calcite	15.3	2.5	0.2	0.5	2.0	0.7	2.8	8.9	-
Dolomite	32.1	39.2	43.4	40.7	2.3	14.7	-	4.1	3.1
TOTAL	47.4	41.7	43.6	41.2	4.3	15.4	2.8	13	3.1
Sulfate minerals									
Gypsum	-	4.1	8.5	6.3	0.7	-	-	-	-
Pyrite	-	0.9	0.5	0.5	-	7.0	-	-	1.2
Sphalerite	-	-	-	-	-	6.2	1.3	-	-
Galena	-	-	-	-	-	2.2	-	-	-
TOTAL		5	9	6.8	0.7	15.4	1.3	--	1.2
Native mineral									
Graphite	2.3	2.1	1.5	0.5	6.7	-	-	-	-
TOTAL	2.3	2.1	1.5	0.5	6.7	-	-	-	-
Inosilicate mineral									
Amphibole	-	-	-	-	-	26.5	59.0	25.5	-
TOTAL	-	-	-	-	-	26.5	59.0	25.5	-
Phyllosilicate (Sheet Silicate minerals)									
Annite	-	0.3	0.0	1.2	3.4	-	-	-	-
Muscovite	24.4	18.1	11.8	19.9	54.8	-	5.9	0.6	-
Chlorite	4.3	-	-	-	19.2	3.2	5.6	16.2	-
Kaolinite	1.8	-	-	-	-	-	-	-	-
TOTAL	30.5	18.4	11.8	21.1	77.3	3.2	11.5	16.8	0.0
GRAND TOTAL	100.0	100.0	100.0	100.0	100.0	100.0	100.0	100.0	100.0



Table 2. In-situ stress, lab testing conditions, and natural fracture orientations of the EGS Collab sites.

In-situ stress of EGS Collab testbeds using information available at time of testing												
Location		Rock type			Depth (m)		Sv (MPa)		SH (MPa)		Sh (MPa)	
E1 4850 level *		Schist (PS01)			1480		44.1		42.6		21.7	
E2 4100 level *		Amphibolite and Rhyolite (YA02)			1250		36		37.3		18.3	
Laboratory testing conditions to simulate in-situ stresses												
Location		$\frac{\sigma_1 - \sigma_3}{2}$		$\frac{\sigma_1 + \sigma_3}{2}$			$\tau_n$ at 30° from $\sigma_1$			$\sigma_n$ at 30° from $\sigma_1$		
E1 4850 level **		10		34			8.7			29		
E2 4100 level **		9		27			7.7			23		
Natural fracture orientations of EGS Collab field sites												
Location		Hydraulic fracture		Joint set 1		Joint set 2		Joint set 3		Foliation		
		Strike	Dip	Strike	Dip	Strike	Dip	Strike	Dip	Strike	Dip	
4100 level		104°	63°	15°	35°	260°	69°	120°	35°	120°	35°	
4850 level		86°	78°	237°	84°	10°	33°	227°	19°	145°	80°	

\* Values presented using current available data when this paper was written;

\*\* Values used for laboratory experiments based on the data that was available at the time of testing.

Table 3. Measured shear strength, permeability enhancement of natural fractures.

Field sites	Feature	Internal Friction Angle/ Cohesion	Theoretical hydroshearing fluid pressure	Actual hydroshearing fluid pressure	Phyllosilicate Content of fractures	Intact permeability	Fracture permeability	Hydroshearing or not	Maximum pore pressure *
E1 Site 4850 level	Intact matrix or bonded fracture	58.7 ( $\pm 0.24$ ) ° 1.6 ( $\pm 0.34$ ) MPa	34 MPa	--	--	--	--	--	28.5 MPa
	PS01-03 (Intact parallel foliation)	41.4 ( $\pm 0.08$ ) ° 3.8 ( $\pm 0.04$ ) MPa	23 MPa	23 MPa	30.5%	<10 <sup>-4</sup> mD	After mechanical shear: 0.2-0.4 mD After hydroshearing: 0-5 mD	Occurred after mechanical shear	
	PS01-06 (Infilled natural fracture)	36 ( $\pm 1$ ) ° 3.24 ( $\pm 0.6$ ) MPa	22 MPa	23.5 MPa	18.4%	<10 <sup>-4</sup> mD	After mechanical shear: 0.01-0.1 mD After hydroshearing: 0.1-1 mD (retainable)	Occurred after mechanical shear	
	PS01-08 (Infilled natural fracture)	41.8 ( $\pm 0.6$ ) ° 4.3 ( $\pm 0.5$ ) MPa	24 MPa**	14.5 MPa **	11.8%	<10 <sup>-3</sup> mD	After mechanical shear: 0.3-1.2 mD After hydroshearing: 4-7 mD (retainable)	Occurred after mechanical shear	
	PS01-09 (Infilled natural fracture)	58 ( $\pm 9.2$ ) ° 15.8 ( $\pm 7.8$ ) MPa	32 MPa	Not occurred	21.1%	10 <sup>-4</sup> -10 <sup>-3</sup> mD	After mechanical shear: 0.002-0.028 mD After hydroshearing: 0.001-0.56 mD (retainable)	Not occurred	
	PS01-11 (Pre-separated weak foliation)	17 ( $\pm 0.5$ ) ° 1.9 ( $\pm 0.5$ ) MPa	6 MPa	7.4 MPa	77.3%	0.2-0.3 mD	After hydroshearing: 0.02-0.03 mD After hydroshearing: 0.002-0.01 mD	Occurred without mechanical shear	
E2 Site 4100 level	YA02-01 (Dark mineral infilled amphibolite)	--	--	Not occurred	3.2%	10 <sup>-4</sup> -10 <sup>-3</sup> mD	After mechanical shear: 0.01-8 mD	Not occurred	22.5 MPa
	YA02-02 (Dark mineral infilled amphibolite)	40 ( $\pm 0.03$ ) ° 8.2 ( $\pm 0.04$ ) MPa	23.2 MPa	--	11.5%	10 <sup>-4</sup> -10 <sup>-3</sup> mD	After mechanical shear: 0.01-0.13 mD	Not tried, but not likely to occur	
	YA02-03 (White mineral infilled amphibolite)	27 ( $\pm 0.24$ ) ° 8.2 ( $\pm 0.18$ ) MPa	24 MPa	--	16.8%	10 <sup>-4</sup> -10 <sup>-3</sup> mD	After mechanical shear: 0.0003-0.002 mD	Not tried, but not likely to occur	
	YA02-04 (Dark mineral infilled rhyolite)	37 ( $\pm 0.12$ ) ° 11.3 ( $\pm 0.1$ ) MPa	27 MPa	--	0	10 <sup>-4</sup> -10 <sup>-3</sup> mD	After mechanical shear: 0.1-0.3 mD	Not tried, but not likely to occur	
	YA02-05 (Pre-separated rhyolite fracture)	42.6 ( $\pm 0.5$ ) ° 5.9 ( $\pm 0.5$ ) MPa	20.5 MPa	20.2 MPa	--	0.3-0.35 mD	After hydroshearing: 0.6-6 mD After hydroshearing: 0.3-0.9 mD	Occurred without mechanical shear	

\* Maximum pore pressure is 0.5 MPa lower than the confining pressure of the experiment.

\*\* Applied shear stress during the experiment was 25 MPa instead of the intended value of 8.7 MPa.

Table 4. Fitted parameters relating confining stress, mechanical aperture, and hydraulic aperture.

Sample ID		Barton-Bandis model				Exponential model			Modified Witherspoon factor $N$		
		$b_{b0}$ (mm)	A (mm/N)	B (N <sup>-1</sup> )	$R^2$	$b_{e0}$ (mm)	$\alpha$ (MPa <sup>-1</sup> )	$R^2$	Regression value	Uncertainty	$R^2$
YA02-02	Loading	0.1388± 3.30e-4	0.0034± 2.86e-5	0.0248± 1.47e-4	1.00	0.1257± 1.49e-4	-0.0145± 3.78e-5	1.00	0.0388	0.0453~ 0.0360	0.74
	Unloading	0.0839± 8.66e-5	0.0008± 4.44e-6	0.01± 4.27e-5	1.00	0.0814± 1.26e-4	-0.0076± 4.54e-5	0.99	0.0400	0.0447~ 0.0376	0.76
YA02-03	Loading	0.1710± 3.94e-4	0.0030± 2.81e-5	0.0174± 1.24e-4	0.99	0.1622± 5.21e-5	-0.0118± 1.05e-5	1.00	0.0097	0.0107~ 0.0864	0.85
	Unloading	0.1416± 8.54e-5	0.0018± 5.22e-6	0.0129± 2.91e-5	1.00	0.1369± 1.48e-4	-0.0094± 3.47e-5	1.00	0.0086	0.0099~ 0.0055	0.81
YA02-04	Loading	0.2033± 3.70e-4	0.0031± 2.36e-5	0.0153± 8.82e-5	1.00	0.1938± 9.86e-5	-0.0105± 1.50e-5	1.00	0.0281	0.0321~ 0.0261	0.80
	Unloading	0.1568± 1.30e-4	0.0014± 6.18e-6	0.0088± 3.21e-5	1.00	0.1531± 2.05e-4	-0.0068± 3.73e-5	0.99	0.0296	0.0349~ 0.0267	0.66

## Figures

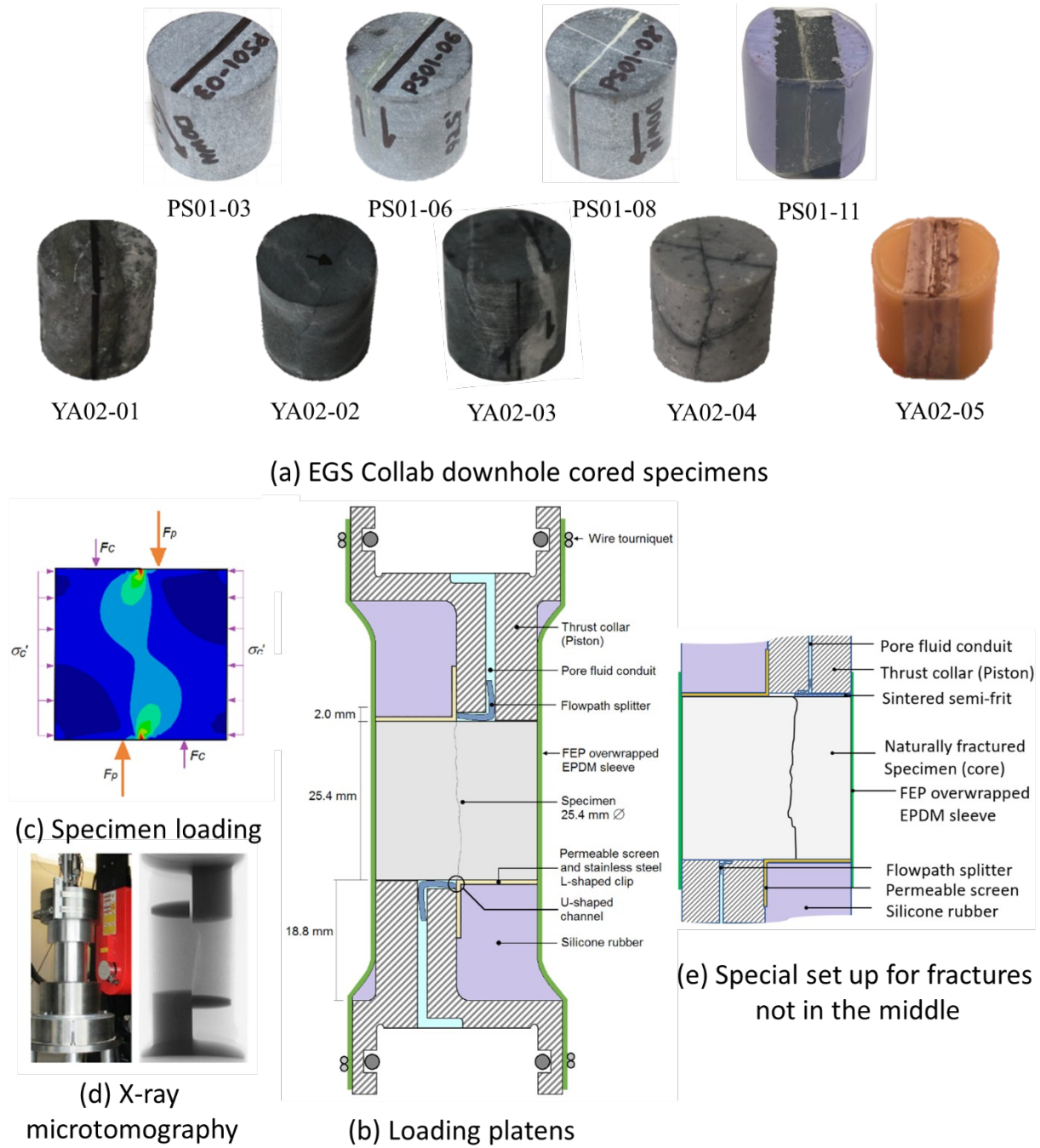


Figure 1. Triaxial direct-shear setup and crystalline specimen drilled from EGS Collab field sites. (a) Care was taken to orient cores parallel to natural fractures and to position the fracture across the diameter of the core, making these samples ideal for triaxial direct-shear testing that targeted suspected weak natural fractures. (b) The naturally fractured specimen is aligned with the direct-shear plane produced by the two opposing half-cylinder pistons. (c) The stress distribution of the sample during the experiment predicted by Abaqus modeling. (d) X-ray imaging setup and greyscale radiograph during an experiment. (e) A stainless steel segment-disk was inserted when needed to ensure initial shear loading across the targeted natural fracture (e.g., YA02-02).

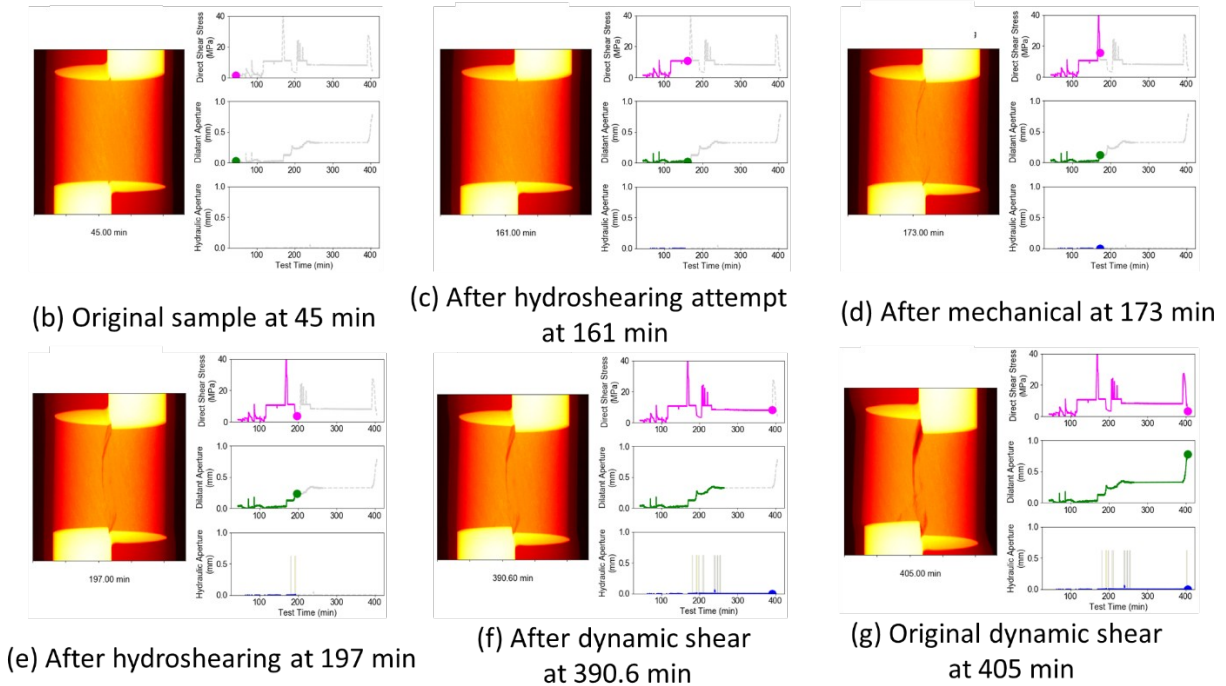
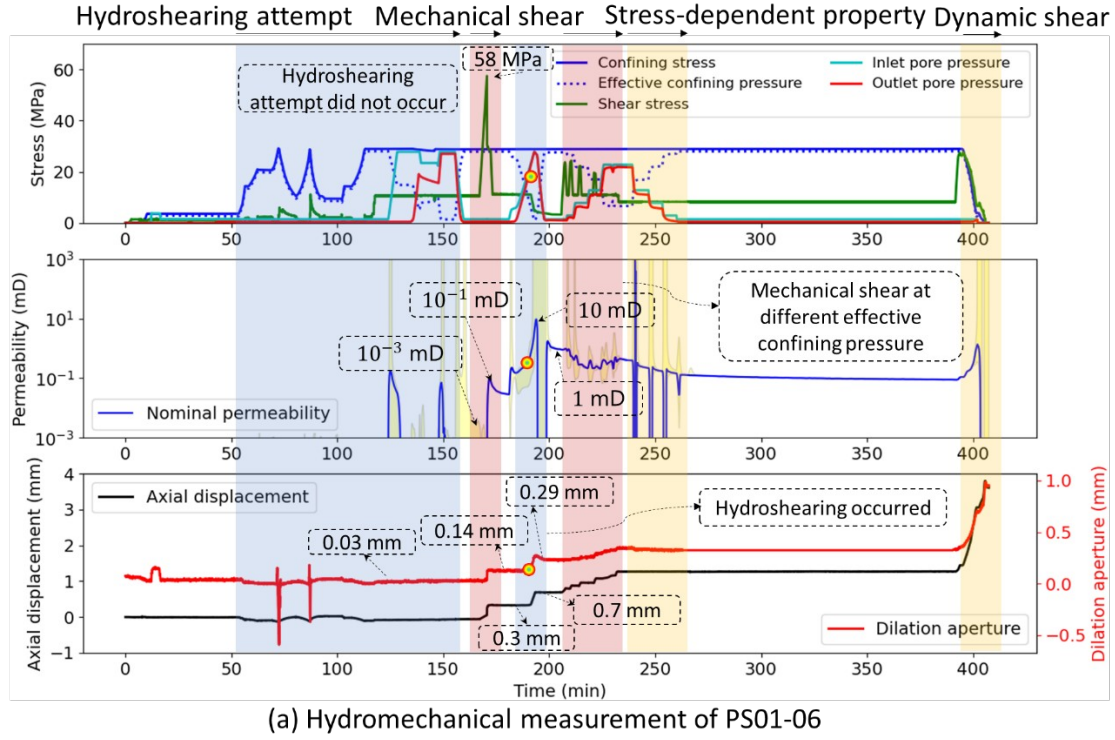


Figure 2. Hydro-mechanical measurement of PS01-06 and 5n-situ x-ray imaging. (a) The upper panel shows the pressures as a function of time. The middle panel shows transient permeability. The bottom panel shows axial displacement and dilation aperture. The highlighted points show the occurrence point of hydroshearing. This test procedure yielded simultaneous natural fracture intact and residual hydro-mechanical properties obtained entirely at in-situ stress conditions, replicated for the EGS Collab Experiment 1 site. (b) This provided valuable confirmation for the state of the sample as the test was underway and provided measurements of the fracture geometry at uninterrupted in-situ stress conditions.

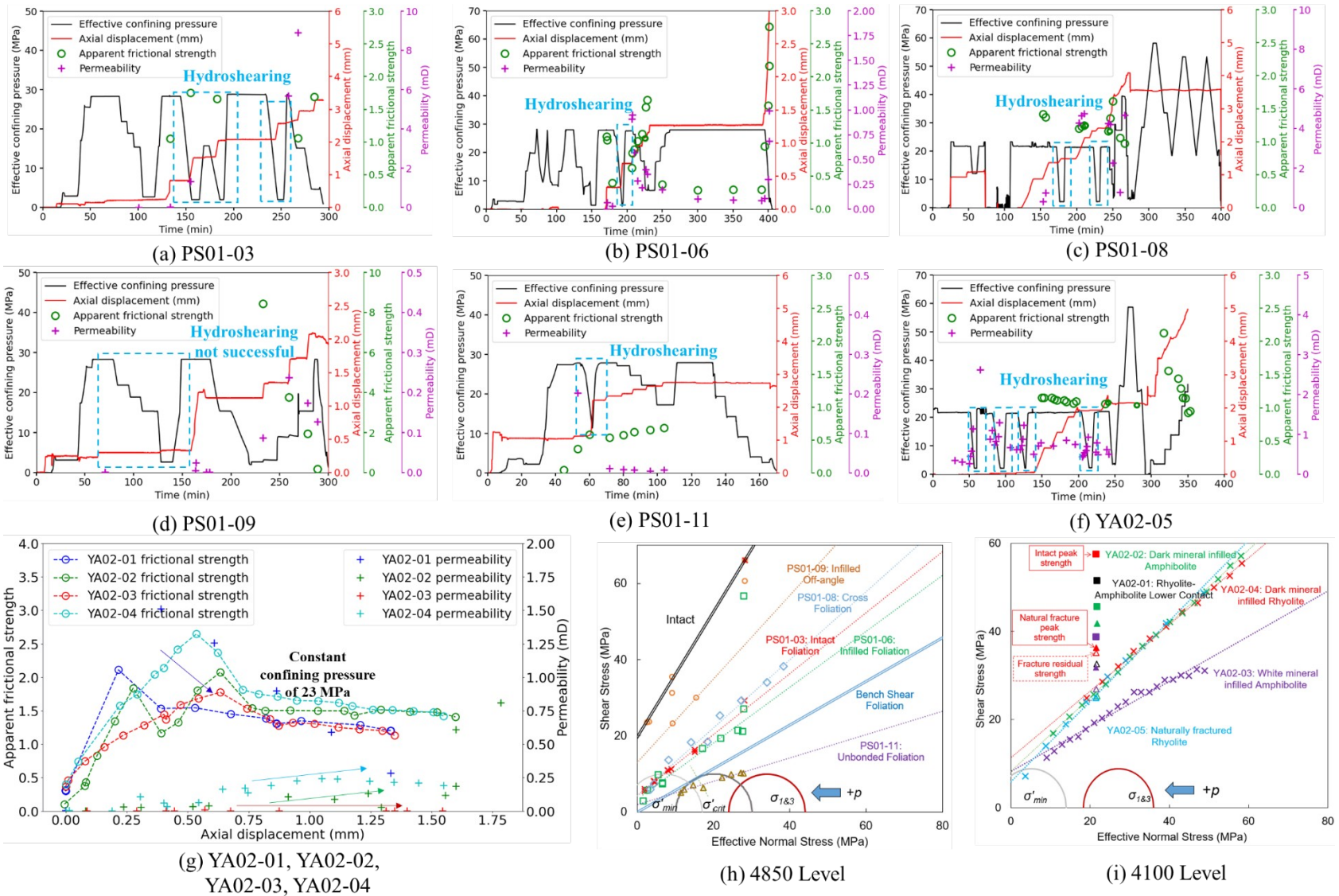


Figure 3. Evolution of permeability and apparent frictional strength for all specimens, and measured triaxial direct-shear stresses in Mohr-Coulomb slip analysis for EGS collab sample. A benchtop gravity slant shear test was used to estimate a Mohr-Coulomb friction angle of  $30^\circ$  and cohesion of 0 MPa for a separated natural foliation fracture of 4850 level.



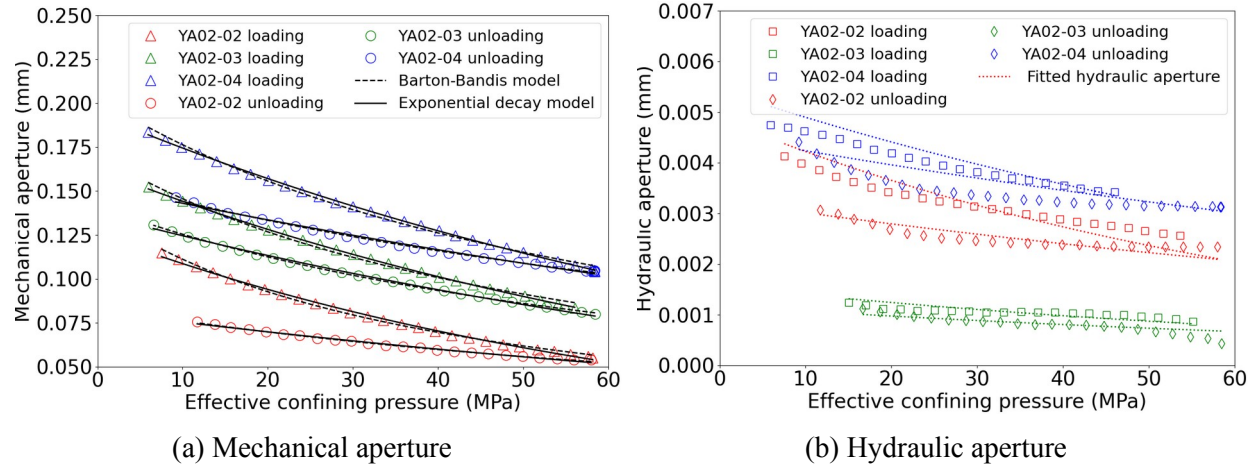


Fig. 4 Relationship between aperture and effective confining pressure

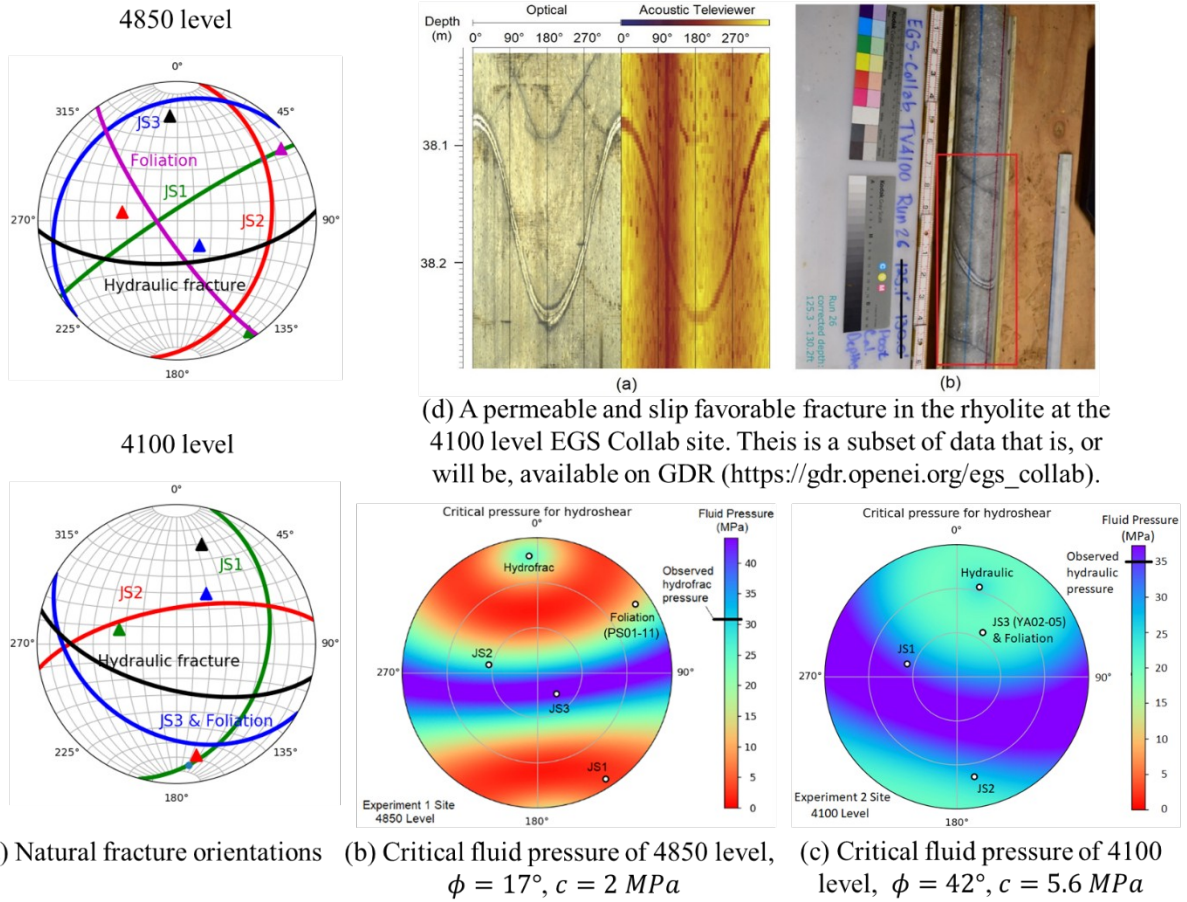


Figure 5. Orientations of natural fractures, lower hemisphere stereoplot of critical fluid pressure to induce hydroshearing, and the selected fracture for in situ hydroshearing.